Solid Freeform Fabrication 2024: Proceedings of the 35th Annual International Solid Freeform Fabrication Symposium – An Additive Manufacturing Conference
Reviewed Paper

PARAMETRIC INVESTIGATION OF SINGLE-LAYER STAINLESS STEEL 316L WITH NOVEL LASER POWDER BED FUSION TECHNOLOGY: DIODE AREA MELTING WITH 450 NM BLUE LASERS

S. C. Erman*, A. Aydin, A. Liang, and K. Mumtaz

Department of Mechanical Engineering, The University of Sheffield, Sheffield, United Kingdom, S1 4BJ

*Corresponding author: scerman1@sheffield.ac.uk

Abstract

Diode Area Melting (DAM) is a novel additive manufacturing technology that contains low optical power (~3.5W) output and lower wavelength (450 nm) lasers compared to traditional laser powder bed fusion (LPBF) with 1064 nm. DAM enables the processing of materials with independently addressable 450 nm blue diode lasers, which are integrated into a multi-laser head. The multi-laser head incorporates focusing and collimating lenses, which facilitate the achievement of localized melting via the connection of multiple 450 nm blue diode lasers with their fiber-coupled output to the head assembly. The use of a shorter wavelength laser in the processing of metal powders using a DAM system has been demonstrated to enhance the power absorptivity of the metals in question previously. DAM has already been utilized to process Ti-6Al-4V through the integration of 450 nm and 808 nm diode lasers. The objective of this study is to demonstrate the production capability of stainless steel 316L (SS316L) using DAM. In this study, a range of scanning speeds (50 to 500 mm/min) and hatch distances (0.2, 0.3, and 0.4 mm) were selected as process parameters to identify the optimal process parameter window for the fabrication of single-layer SS316L structures in terms of melt pool characterization and surface roughness measurements. The findings indicated that the surface roughness of samples with a 0.2 mm hatch distance was observed to be lower in comparison to other samples at each scanning speed. Furthermore, the surface roughness of samples lower than 15 μm ranged between 25.6-126 J/mm^2 even 3.469 μm for 126 J/mm^2.

Keywords: Diode Area Melting (DAM), Laser Powder Bed Fusion (LPBF), SS316L

1. Introduction

Currently, traditional laser powder bed fusion (LPBF) is a well-known additive manufacturing approach to create complex structures with good mechanical properties and surface quality via melting metal powder with laser energy [1]. Diode Area Melting (DAM) is a novel additive manufacturing technology that contains low power (3.5W) and lower wavelength (450 nm) blue diode lasers compared to LPBF. This paper presents the use of DAM as an alternative method to laser-based processing systems. DAM comes with several advantages in nature compared to traditional LPBF systems. These are lower power requirements with independently triggered multi-blue diode lasers, high resolution during the manufacturing process, power efficiency with using lower wavelength lasers by increasing material absorbance, and scalability for large scanning areas [2]. Previously, DAM was studied with 808 nm diode lasers with Ti-6Al-4V [3], [4] and stainless steel 316L, (SS316L) [5], [6] and 450 nm blue diode lasers were used for Ti-6Al-4V processing recently [7]. DAM enables processing with 450 nm blue diode lasers that help to increase the power absorptivity of metals in DAM [4].

The knowledge of the DAM process is limited with Ti-6Al-4V [3], [4], [7], there is only one work that focuses on another material to process (SS316L) in DAM with different wavelength lasers (808 nm) [5]. For the first time, the morphology of single-track SS316L samples fabricated by DAM is published in this paper. The single-track study in this paper helps to specify process parameters for single-layer experiments. Consequently, at first detailed study is wanted to be performed with standard material, SS316L, for additive manufacturing to create a comparable data set with traditional LPBF. SS316L is a highly preferable material due to its superior strength and corrosion resistance in LPBF applications [8]. Also, stainless steel 316L has a general usage in several industries. In addition to medical implants and marine engineering applications due to its outstanding corrosion and oxidation capability [9]; lock components and fasteners in the automotive industry, pipe flange clamps and window hardware in industrial applications, and photographic equipment are some examples of SS316L usage in different industries [8].

SS316L is investigated in this work and the absorbance of powder is increased up to 10% according to literature work [10] using 450 nm wavelength instead of 1064 nm. For the first time in this paper, 450 nm diode lasers are implemented to process SS316L powder. Foremost, a parametric study is conducted to produce single-track structures with different scanning speeds. After that, a hatch distance study is performed with different scanning speeds and melt pool overlaps. Then, the effect of laser track overlap percentage and scanning speed is investigated on top surface roughness and melt pool width/depth characterization of single layer samples. Surface roughness is defined as a measure of the texture of a surface, quantifying its irregularities and it is widely used in literature to evaluate the part quality and optimize process parameters [11], [12], [13]. Finally, surface roughness for single-layer SS316L is investigated in terms of surface energy density (SED) calculations.

2. Materials and Methods

In the DAM process, multiple and independently addressable 450 nm blue diode lasers are utilized to melt metal powder to fabricate 3D net shape samples. During the process, the laser array head which contains more than 100 spots for positioning independent lasers moves through the intended scanning path and melts the powder. Figure 1 clearly shows the configuration of the laser array and DAM process schematically. The details of the process can be investigated in previous work from our research lab [3], [7]. In this work, only 6 lasers are used to observe the small-scale processing capacity of new material for this system (see Figure 2(a)). A zigzag scanning pattern is employed to fabricate thirty different single-layer samples (6x4 mm^2). Figure 2(c) illustrates the experimental design, including the dimensions of the samples and the scanning strategy employed. Lasers are mounted into a water-cooling plate that has been designed to maintain a temperature of no more than 30°C during operation. This ensures that the lasers are used in an optimal operational temperature range. Then, it is validated by in-situ thermal camera measurement experimentally.

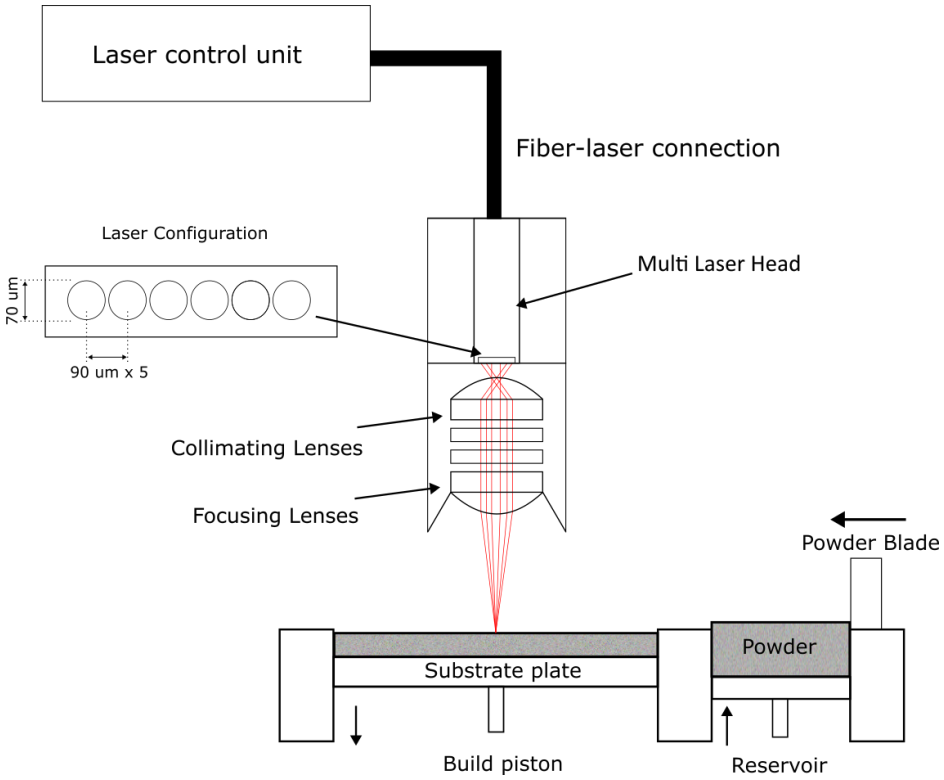

Figure 1: The schematic view of the Diode Area Melting process.

Lasers are elongated via an external fiber cable to the multi-laser head. There are both collimating and focusing lenses inside the multi-laser head. Beams are aligned and focused thanks to going through these lenses. At the final, laser beams are focused on a single line over a substrate plate (see Figure 2(b)). The spot size of each laser is 70 µm during full focus but this changes according to the position of the multi-laser head assembly over the substrate, which is 27 mm for our multi-laser head, i.e., focus distance. Also, the spacing between each laser centre is 90 µm which can be seen in Figure 2(a).

The spacing between each laser track is important to eliminate the lack of fusion error during the manufacturing process. Hatch distance should not be specified too much to fabricate fully dense parts. This can create holes between laser tracks. Also, an increase in the overlap between subsequent laser tracks increases the number of laser tracks to manufacture parts. The surface roughness can be affected negatively by that [14]. In this study, different overlap percentage (20, 40, and 60%) values according to the length of the fiber array which is calculated from the laser beam profile. This approach helps to understand the amount of melt pool overlap on top surface roughness. Figure 2(a) schematically represents the laser configuration and Figure 2(b) shows the optical profile of the laser array in this work. According to profilometer analysis which is performed with NanoScan 2s Pryo/9/5 total width of the laser beams equals 526 µm (see Figure 2(b)).

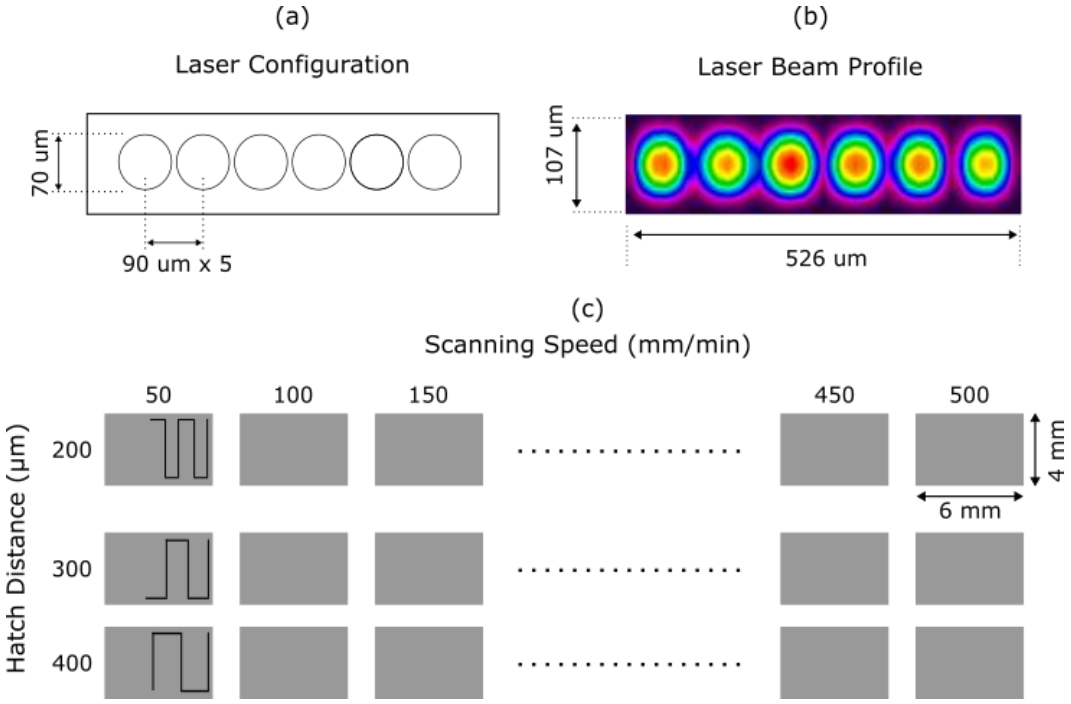

Figure 2: (a) Laser configuration, (b) laser beam profile of 6 lasers, (c) experimental design with sample dimensions and scanning strategy.

Table 1: All process parameters in this work.

Scanning Speed (mm/min)	50,100,150,200,250,300,350,400,450,500
Hatch Distance (µm)	200,300,400
Laser power (W)	3.5 x 6

Table 1 shows all process parameters in this paper. In this work, multiple 3.5 W blue diode lasers are used to melt SS316L powder. In this paper, a 1 mm thick layer thickness is specified intentionally to show the penetration depth of the samples according to given energy. Scanning speed (SS) and hatch distance (HD) are two main process parameters. Scanning speed varies between 50 mm/min to 500 mm/min by 50 increments. Another process parameter is hatch distance which is selected according to the configuration of the laser beam profile obtained from the optical profilometer. Therefore, hatch distance values for single-layer experiments are calculated from the total width of the beam which corresponds to around 20, 40, and 60% (400, 300, and 200 µm hatch distances – HD400, HD300, HD200) overlap. A hatch distance study is performed to characterize the melt pool width and depth of samples that are fabricated from a special laser configuration in this work. Also, the effect of hatch distance and scanning speeds on surface roughness is investigated.

In this work, SS316L powder by Carpenter Additive is selected as a feedstock material. The particle size distribution of powder changes between 20.8 µm (D_{10}) and 49.8 µm (D_{90}). Figure 3 shows SS316L powder morphology under 500x magnification. In the chemical composition of this austenitic steel, chromium (17.6%), molybdenum (2.34%), and nickel (12.6%) elements that are provided from the test certificate of powder batch play an important role. For instance, the molybdenum amount increases the corrosion resistance [15] and the chromium and nickel amount

limits the possibility of occurring sigma and ferrite phases and ensures the austenitic phase in 316L [15]. Table 2 shows the composition of the powder batch which is provided by the supplier.

Table 2: The chemical composition of SS316L powder.

Elements	C	Cr	Fe	Mn	Mo	Ni	Si	Others
Weight (%)	0.016	17.6	Balance	0.89	2.34	12.6	0.57	0.13

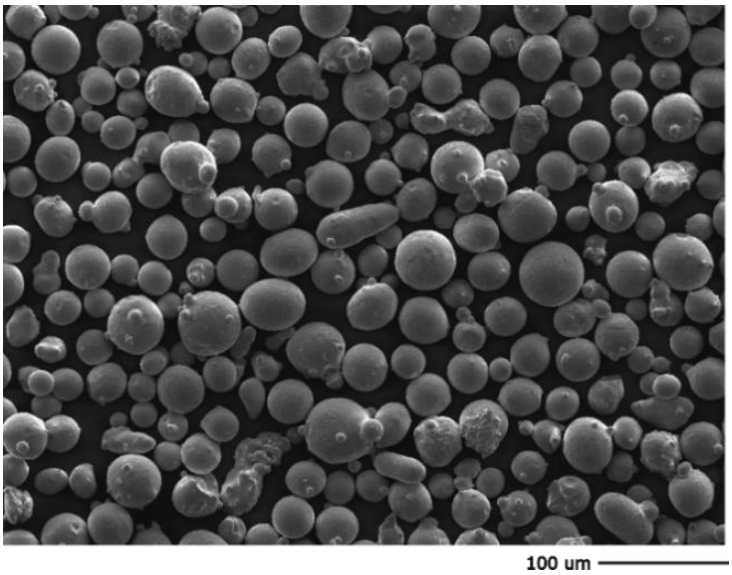

Figure 3: SS316L powder morphology.

The top surface roughness of samples is measured with Alicona Infinite Focus SL optically. Samples are mounted into Bakelite by Buehler Simplimet hot mounting machine to ensure surface flatness before microscopy investigation. After that sample surfaces are grinded by using P320-P4000 waterproof grinding papers on Buehler Automet grinding machine. 0.06 μm particle-sized colloidal silica is used for polishing and samples are rinsed with isopropanol. Microscopy investigation is conducted after surface roughness measurements from both the top surface and cross-section for single-layer samples and from cross-section for single-track samples under 5x magnification. Finally, the surface energy density (SED) formula is defined as [16],

$$E_s = \frac{P}{SS*HD} \quad (1)$$

where *P* is total laser power, *SS* is scanning speed, and *HD* is hatch distance is employed to evaluate top surface roughness in terms of energy density.

3. Results

Figure 4 shows cross section of all single-track samples from SS50 to SS500. It is observed that penetration depth and width decrease with an increase in scanning speeds. Also, it is seen that the melt pool shape looks like a crescent at SS50 (see Figure 4(a)). Melt pool width starts to enlarge both SS100 and SS150 (see Figures 4(b) and (c)). After SS200 to SS350 the curvature of the top part of the melt pool increases and starts to turn round shape. After SS400 to SS500 melt pool shape transforms totally to a spherical shape. Later in this paper, cross-section micrographs of

single-layer samples under 5x magnification are presented with different scanning and hatch distances (see Figure 6). The melt pool track on single-layer samples is narrow compared to single track due to melt pool overlap that can be seen in Figure 4(a) to (j). For instance, the melt pool width of a single-track sample in Figure 4(a) is more than 500 μm, the melt pool width of the single-layer sample with SS50 is less than 400 μm for HD400, around 300 μm and 200 μm for HD300, and HD200 respectively (see Figure 5(p)) due to overlapping. There is no overlap on a single scan, therefore melt pool width is wider than a single layer that contains melt pool overlap.

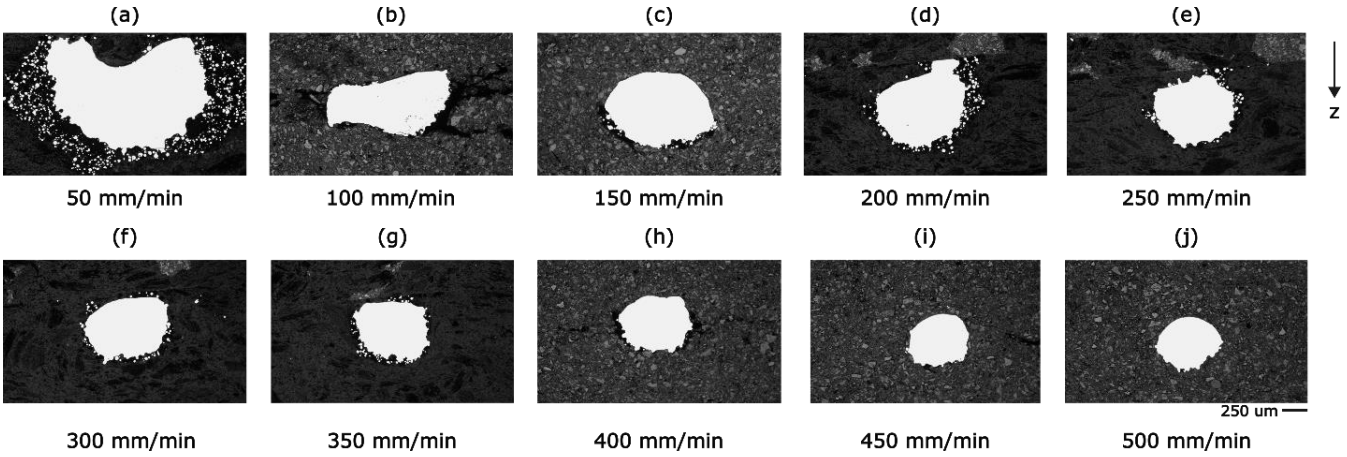

Figure 4: Optical micrograph from a cross-section of single-track samples.

Figure 5 shows micrographs that are taken from the top surface of the samples. Micrographs in Figure 5 start from 50 mm/min to 250 mm/min (SS50 and SS250) for each hatch distance (HD200, HD300 and HD400). It is seen in Figure 5(a) to (c) [(d) to (f), (g) to (i), (j) to (l), and (m) to (o)] and Figure 5(p) that melt pool width increases when hatch distance increases. Also, melt pool width reaches its maximum values at SS150 for HD300 and HD400, and at SS200 for HD200 as can be seen in Figure 5(p). It is thought that given energy input at low scanning speed is higher compared to higher speed. Therefore, high energy inputs (for example, 126 J/mm^2 for SS50/HD200 and 84 J/mm^2 for SS50/HD300 are explicitly represented in Table 3) create a deeper melt pool, and this leads to a narrow melt pool width (see Figure 5(p) up to SS150 and SS200). As the scanning speed exceeds the upper limit for the optimum process parameter window, the melt pool width decreases due to the reduction in energy density (see Figure 5(p) after SS150). This is because, as the scanning speed increases, the energy density decreases without a corresponding change in the other process parameters (see Equation (1)).

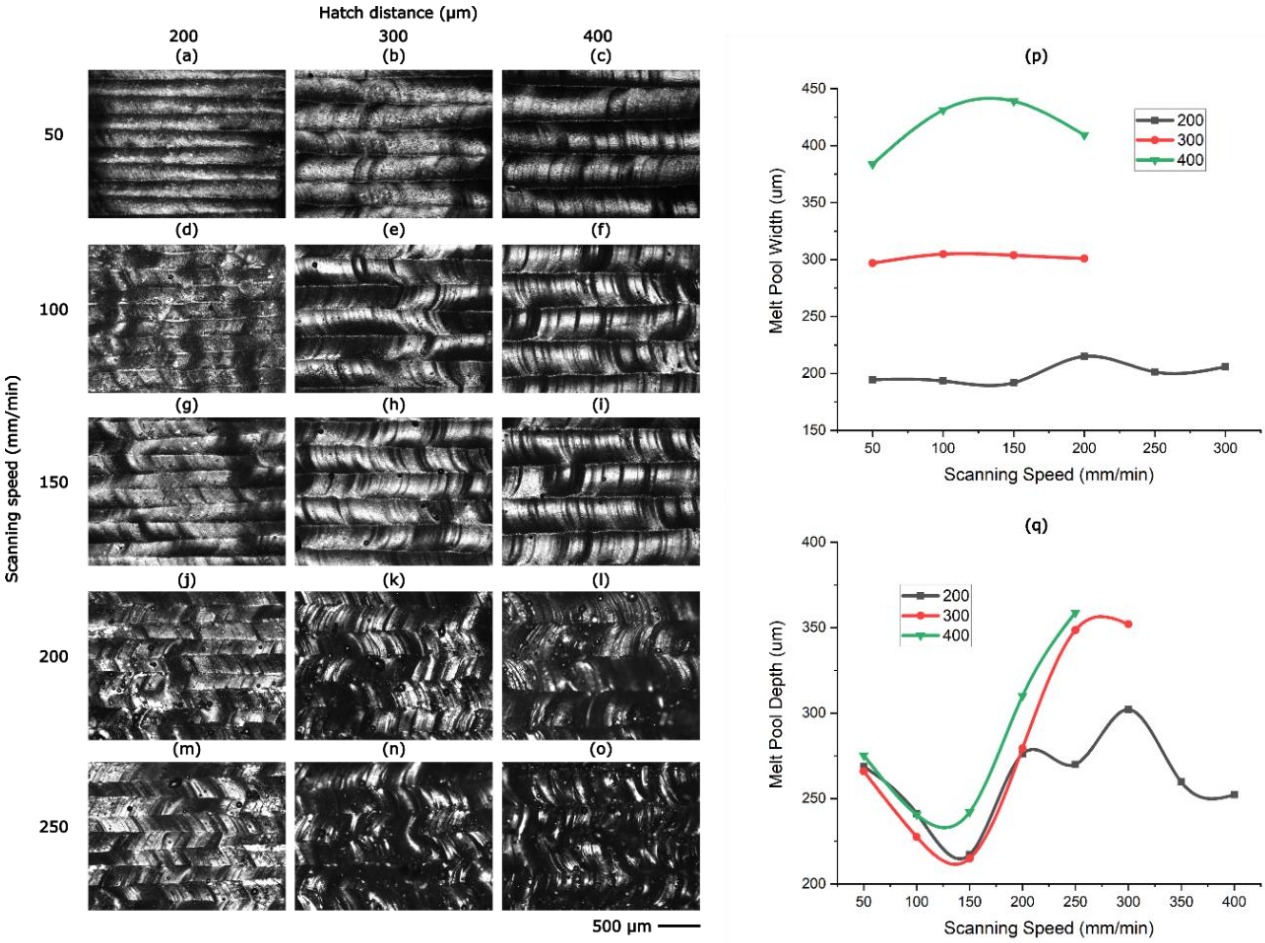

Figure 5: (a)-(o) Optical micrographs from the top surface of samples, (p)/(q) melt pool width/depth changing over scanning speed at both hatch distances (200, 300, and 400 µm).

Figure 5(p) shows the melt pool width trends for both hatch distance sets. The width and depth of the melt pools were measured from optical micrographs, as illustrated in Figures 5 and 6. Ten measurements were taken from each micrograph, and the averaged values for the melt pool width and depth are presented in Figures 5(p) and (q), respectively. Melt pool width reaches 215.01, 304.79, and 439.07 µm at maximum respectively for HD200, HD300, and HD400. After SS200, it is unable to detect melt pool width under optical microscopy correctly due to several spatters (see Figure 5(k)-(l) and (n)-(o)) for both HD300 and HD400. Consequently, further micrographs are not shown here.

Figure 5(q) only shows the melt pool depth of fully melted and continuous samples. After SS400 for HD200, SS300 for HD300, and SS250 for HD400, discontinuity and balling defects become dominant. It is for this reason that the width of the melt pool of samples after SS400/SS300/SS250 for HD200/HD300/HD400 is not displayed in Figure 5(q).

Figure 6 shows optical micrographs from a cross-section of samples for SS50, SS150, SS250, and SS500. It is seen that melt pool depth decreases from SS50 to SS150 and increases after SS150. Melt pool depth decreases from 268.82 to 217.29 µm for HD200, from 265.98 to 214.95 µm for HD300, and from 275.28 to 242.18 µm for HD400 between SS50 to SS150 (see

Figure 5(q)). The top surface of the melt pool in Figure 6(a)-(e) is flat compared to other samples. Orange vertical dotted lines shown in Figure 6(c) emphasize the crescent effect on the sample surface due to lack of overlapping. It can be said that HD400 (% 20 overlap of the laser beam) is not enough to create a flat surface. After SS250 balling starts to become dominant, especially for HD300 and HD400 results (see Figure 6(h)-(l)) and the surface transforms from flat to curved structure. Also, the initiation of discontinuities is shown in Figure 6(i) with green dotted circles. Further discontinuities also be seen in Figure 6(k) and (l) with dotted green circles.

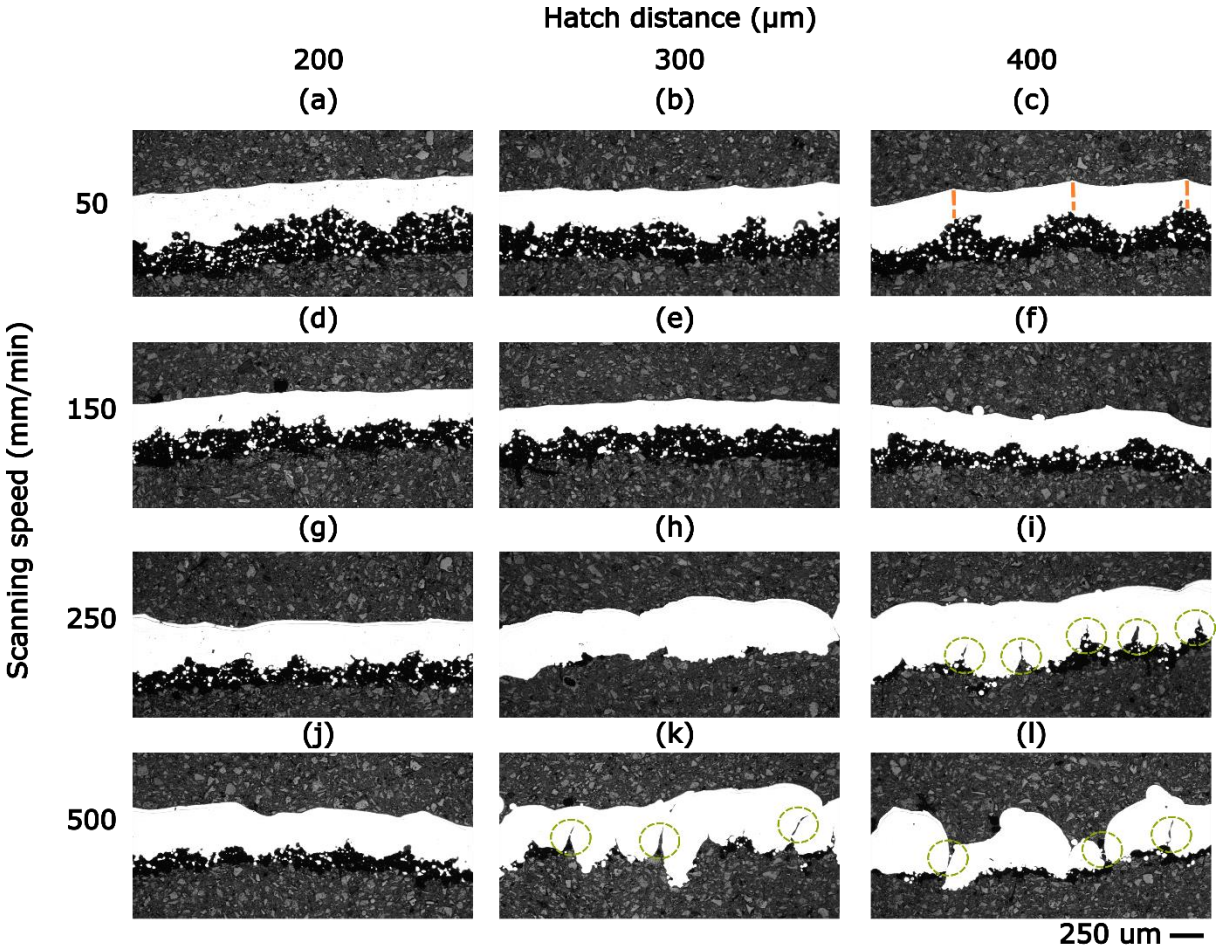

Figure 6 : (a)-(l) Optical micrographs from cross-sections of samples.

Consequently, according to melt pool characterization and optical microscopy images from both top surfaces and cross-sections of samples, the optimum process parameters for single-layer SS316L parts is HD200 for hatch distance which corresponds to 60% laser beam overlap and SS200 and below (SS50, SS100, SS150) for scanning speed. The production of fully melted single-layer samples devoid of balling defects and holes is achieved through the utilization of HD200 and below SS200 as the hatch distance and scanning speed, respectively. A reduction in hatch distance, which increases the volume of laser tracks that overlap, can be considered to act as a reheating process. This phenomenon is of considerable importance in the fabrication of samples [17].

Successfully melted and bonded parts are fabricated for high speeds (such as SS250 to SS500) and low laser beam overlaps (HD300 and HD400) process parameters, these samples can

contain minor defects such as holes due to poor overlap and balling due to low energy input. Figures 5(p) and (q) illustrate the influence of hatch distance and scanning speed on the width and depth of the melt pool, respectively. Subsequently, the impact of process parameters on the fabrication process is evaluated through the analysis of surface roughness measurements.

Figure 7 shows surface roughness (Ra) values for both scanning speeds (SS50-SS500) and hatch distances (HD200, HD300, and HD400). It is seen that surface roughness increases when scanning speed rises for all hatch distance values. Also, it is shown in Figure 7 that minimum surface roughness values are obtained with HD200 in all scanning speed values. Minimum Ra values are 3.469, 6.577, and 11.106 µm with SS50/SS50/SS100 for HD200-HD300-HD400. Several surface maps are shown in Figure 7.

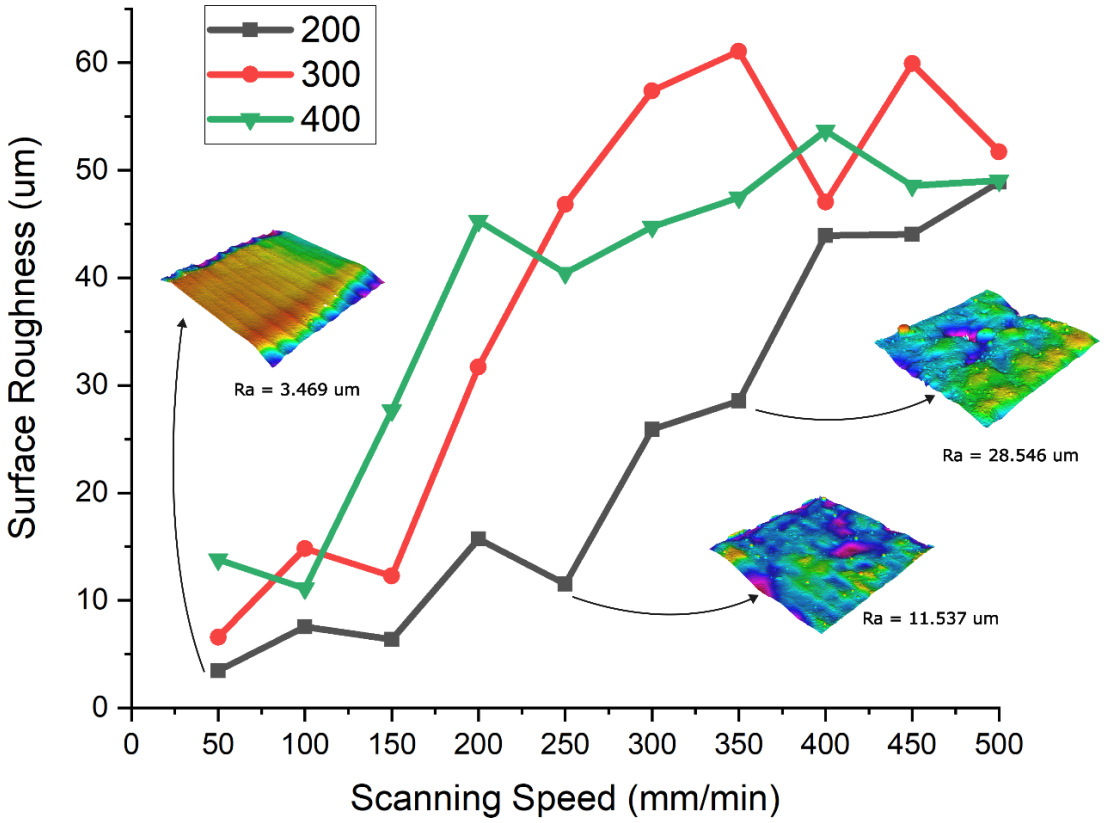

Figure 7: Surface roughness (R_a) for all samples.

Ra values for both hatch distance sets for high speeds such as SS250-SS500 are too high compared to low speeds due to balling and discontinuity thanks to low energy input. The balling phenomenon is more apparent at lower energy density values and the uniformity and continuity of the melt track are compromised by the balling defect [18]. Ra values fluctuate around 3 to 15 for HD200 at SS50 to SS250. Surface roughness increases with scanning speed in this range due to spattering on the surface. The reason for an increase in surface roughness at HD300 and HD400 with scanning speed is an insufficient amount of melt pool overlap. It can be compensated at low speeds due to high energy input (such as 126, 84, 63 J/mm^2) but energy input decreases at high scanning speeds. Therefore, surface roughness increases drastically after SS150 both HD300 and HD400. This increase cannot be explained by spattering (the size of powder changes between 15-

45 µm overall). Following the SS250, the surface roughness values exhibited an excessive increase in comparison to the literature about LPBF works involving SS316L [19], [20].

Table 3: Surface energy density (SED) calculation for all process parameters set.

Process Parameters		Surface Energy Density (J/mm^2)	Surface Roughness (Ra, µm)
SS (mm/min)	HD (µm)		
50	200	126	3.469
50	300	84	6.577
50	400	63	13.814
100	200		7.534
100	300	42	14.824
150	200		6.380
100	400	31.5	11.106
200	200		15.720
150	300	28	12.259
250	200	25.2	11.537
150	400	21	27.680
200	300		31.713
300	200		25.893
350	200	18	28.546
250	300	16.8	46.810
200	400	15.75	45.278
400	200		43.921
300	300	14	57.379
450	200		44.043
250	400	12.6	40.435
500	200		48.887
350	300	12	61.062
300	400	10.5	44.756
400	300		47.025
450	300	9.333	59.907
350	400	9	47.466
500	300	8.4	51.718
400	400	7.875	53.665
450	400	7	48.572
500	400	6.3	49.060

Finally, the correlation between surface roughness and surface energy density (SED) calculation was investigated in this section. Table 3 shows the SED calculation for each process parameter set. In this work, the layer thickness was kept the same during all experiments, so it was aimed to understand the effect of scanning speed (SS) and hatch distance (HD) only on energy density calculations. Some samples have the same energy density because the multiplication of hatch distance and scanning speed gives the same results (e.g., SS50-HD400 and SS100-HD200, SS150-HD400, and SS300-HD200) in the SED formula. It is seen that surface roughness results

are similar in the same energy states (the maximum difference is 8.444 μm at SS100-HD300 and SS150-HD200 which is 42 J/mm^2 energy state). Nevertheless, a minor energy difference is observed between the SS250/HD400 and SS350/HD300 sets with values of 12.6 and 12 J/mm^2 respectively (see Table 3). Additionally, a notable difference in surface roughness is evident, with values of 40.435 μm and 61.062 μm, respectively. It can be observed that there is no consistent correlation between surface roughness results and lower surface energy density values. It is hypothesized that elevated scanning speeds or increased hatch distance parameters may individually impair the surface quality. Consequently, SED values are employed to elucidate the impact of their multiplication.

Figure 8 shows variation in surface roughness compared to the decreasing order of SED values. It is observed that when energy density decreases, averaged surface roughness increases. The optimum surface energy density (SED) interval is between 25.6-126 J/mm^2 for SS316L single-layer samples in terms of surface roughness which is around 10 μm at maximum. Below 25.6 J/mm^2 surface roughness increases drastically. While surface roughness results fluctuate around 50 μm in the region where SED values are between 16.8-6.3 J/mm^2 . The surface roughness results after SS250 for both hatch distance values (corresponding to low SED values in Figure 8) look noisy. It is thought that the surface roughness values are higher at higher scanning speeds due to the high number of spatters and balling defects. There is no time for the powder to melt properly with the laser and discontinuity is observed at high scan speeds [21]**.**

A review of the literature reveals a paucity of studies utilizing the SED calculation to examine surface roughness and sample quality for manufacturing defects in the context of LBPF. Aqilah et al. [22] examined the surface roughness of LPBF SS316L samples concerning various process parameters, including laser power, scanning speed, and hatch distance. The research findings indicate that an energy density value of 1.667 J/mm^2 represents the optimal parameter for surface roughness, when the laser power is 120 W, the scanning speed is 900 mm/s, and the hatch distance is 0.08 mm. This value was determined through experimental analysis, with a resulting value of 5.53 μm [22]. It is evident that there is a significant discrepancy between the optimum SED values in terms of melt pool characterization and surface roughness of DAM samples with LPBF samples, with a difference of nearly 75 times. It is hypothesized that a more robust formulation is required to facilitate a fair and accurate comparison between DAM and LPBF samples in terms of energy density calculations in future studies.

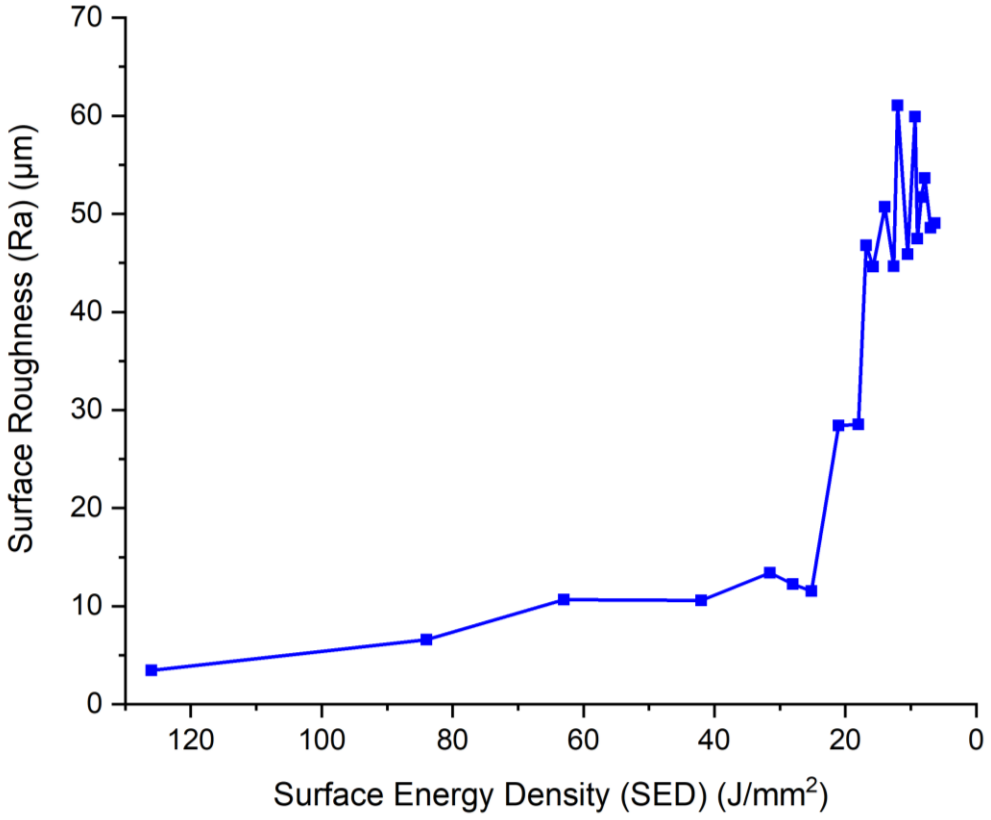

Figure 8: Surface roughness (Ra) distribution along Surface Energy Density (SED) calculation for each energy state.

4. Conclusion

In this work, single track and single layer samples are fabricated via 450 nm blue diode lasers successfully. This investigation reveals the potential of DAM with 450 nm lasers to create fully melted SS316L parts. This study focuses on melt pool characteristics and top surface roughness of single-layer samples with different scanning speeds and hatch distances. It has been demonstrated that the optimal process parameters for the production of SS316L single-layer structures are HD200 and below SS200 in terms of hatch distance and scanning speed, respectively, as determined by melt pool characterization and surface roughness measurements. In consideration of the top surface roughness results, it can be posited that the process parameters HD200 (corresponding to 60% laser beam overlap) and SS50 represent the optimal parameters for hatch distance and scanning speed in the context of this work. Also, surface roughness results were discussed according to surface energy density (SED) calculations. It is stated that the optimum SED interval for SS316L is between 25.6 and 126 J/mm^2. Furthermore, the minimum surface roughness result is obtained as 3.469 µm at 126 J/mm^2. A promising avenue for future research is to conduct more comprehensive energy density calculations to examine the mechanical and microstructural properties of SS316L single-layer structures.

Acknowledgment

This study was completed with support from the Turkish Government Ministry of Education.

REFERENCES

[1] E. M. Sefene, 'State-of-the-art of selective laser melting process: A comprehensive review', *J. Manuf. Syst.*, vol. 63, pp. 250–274, Apr. 2022, doi: 10.1016/j.jmsy.2022.04.002.

[2] M. Zavala-Arredondo *et al.*, 'Laser diode area melting for high speed additive manufacturing of metallic components', *Mater. Des.*, vol. 117, pp. 305–315, Mar. 2017, doi: 10.1016/j.matdes.2016.12.095.

[3] M. Alsaddah, A. Khan, K. Groom, and K. Mumtaz, 'Diode area melting of Ti6Al4V using 808 nm laser sources and variable multi-beam profiles', *Mater. Des.*, vol. 215, Mar. 2022, doi: 10.1016/j.matdes.2022.110518.

[4] M. Alsaddah, A. Khan, K. Groom, and K. Mumtaz, 'Use of 450-808 nm diode lasers for efficient energy absorption during powder bed fusion of Ti6Al4V', doi: 10.1007/s00170-021-06774-4/Published.

[5] M. Zavala-Arredondo, K. M. Groom, and K. Mumtaz, 'Diode area melting single-layer parametric analysis of 316L stainless steel powder', *Int. J. Adv. Manuf. Technol.*, vol. 94, no. 5–8, pp. 2563–2576, Feb. 2018, doi: 10.1007/s00170-017-1040-4.

[6] M. Zavala-Arredondo, H. Ali, K. M. Groom, and K. Mumtaz, 'Investigating the melt pool properties and thermal effects of multi-laser diode area melting', *Int. J. Adv. Manuf. Technol.*, vol. 97, no. 1–4, pp. 1383–1396, Jul. 2018, doi: 10.1007/s00170-018-2038-2.

[7] H. Caglar, A. Liang, K. Groom, and K. Mumtaz, 'Multi-laser powder bed fusion of Ti6Al4V: Diode area melting utilizing low-power 450 nm diode lasers', *J. Mater. Process. Technol.*, vol. 325, Apr. 2024, doi: 10.1016/j.jmatprotec.2024.118303.

[8] P. K. Samal and J. W. Newkirk, *ASM Handbook, Volume 7: Powder Metallurgy*. 1998.

[9] G. F. Sun *et al.*, 'Laser metal deposition as repair technology for 316L stainless steel: Influence of feeding powder compositions on microstructure and mechanical properties', *Opt. Laser Technol.*, vol. 109, pp. 71–83, Jan. 2019, doi: 10.1016/j.optlastec.2018.07.051.

[10] B. Brandau, A. Da Silva, C. Wilsnack, F. Brueckner, and A. F. H. Kaplan, 'Absorbance study of powder conditions for laser additive manufacturing', *Mater. Des.*, vol. 216, Apr. 2022, doi: 10.1016/j.matdes.2022.110591.

[11] U. Ali *et al.*, 'Identification and characterization of spatter particles and their effect on surface roughness, density and mechanical response of 17-4 PH stainless steel laser powder-bed fusion parts', *Mater. Sci. Eng. A*, vol. 756, pp. 98–107, May 2019, doi: 10.1016/j.msea.2019.04.026.

[12] S. Greco, K. Gutzeit, H. Hotz, B. Kirsch, and J. C. Aurich, 'Selective laser melting (SLM) of AISI 316L—impact of laser power, layer thickness, and hatch spacing on roughness, density, and microhardness at constant input energy density', *Int. J. Adv. Manuf. Technol.*, vol. 108, no. 5–6, pp. 1551–1562, May 2020, doi: 10.1007/s00170-020-05510-8.

[13] B. Song, S. Dong, B. Zhang, H. Liao, and C. Coddet, 'Effects of processing parameters on microstructure and mechanical property of selective laser melted Ti6Al4V', *Mater. Des.*, vol. 35, pp. 120–125, Mar. 2012, doi: 10.1016/j.matdes.2011.09.051.

[14] J. A. Cherry, H. M. Davies, S. Mehmood, N. P. Lavery, S. G. R. Brown, and J. Sienz, 'Investigation into the effect of process parameters on microstructural and physical properties of 316L stainless steel parts by selective laser melting', *Int. J. Adv. Manuf. Technol.*, vol. 76, no. 5–8, pp. 869–879, Feb. 2015, doi: 10.1007/s00170-014-6297-2.

[15] A. J. Sedriks, 'Corrosion resistance of austenitic Fe-Cr-Ni-Mo alloys in marine environments', *Int. Met. Rev.*, vol. 27, no. 1, pp. 321–353, Jan. 1982, doi: 10.1179/imr.1982.27.1.321.

[16] M. Ahmed Obeidi *et al.*, ‘Comprehensive assessment of spatter material generated during selective laser melting of stainless steel’, *Mater. Today Commun.*, vol. 25, Dec. 2020, doi: 10.1016/j.mtcomm.2020.101294.
[17] T. H. Hsu *et al.*, ‘Effect of processing parameters on the fractions of martensite in 17-4 PH stainless steel fabricated by selective laser melting’, *J. Alloys Compd.*, vol. 859, Apr. 2021, doi: 10.1016/j.jallcom.2020.157758.
[18] W. Yuan, H. Chen, T. Cheng, and Q. Wei, ‘Effects of laser scanning speeds on different states of the molten pool during selective laser melting: Simulation and experiment’, *Mater. Des.*, vol. 189, Apr. 2020, doi: 10.1016/j.matdes.2020.108542.
[19] D. Wang, Y. Liu, Y. Yang, and D. Xiao, ‘Theoretical and experimental study on surface roughness of 316L stainless steel metal parts obtained through selective laser melting’, *Rapid Prototyp. J.*, vol. 22, no. 4, pp. 706–716, Jun. 2016, doi: 10.1108/RPJ-06-2015-0078.
[20] H. H. Alsalla, C. Smith, and L. Hao, ‘Effect of build orientation on the surface quality, microstructure and mechanical properties of selective laser melting 316L stainless steel’, *Rapid Prototyp. J.*, vol. 24, no. 1, pp. 9–17, Jan. 2018, doi: 10.1108/RPJ-04-2016-0068.
[21] R. Li, J. Liu, Y. Shi, L. Wang, and W. Jiang, ‘Balling behavior of stainless steel and nickel powder during selective laser melting process’, *Int. J. Adv. Manuf. Technol.*, vol. 59, no. 9–12, pp. 1025–1035, Apr. 2012, doi: 10.1007/s00170-011-3566-1.
[22] D. N. Aqilah, A. K. Mohd Sayuti, Y. Farazila, D. Y. Suleiman, M. A. Nor Amirah, and W. B. Wan Nur Izzati, ‘Effects of process parameters on the surface roughness of stainless steel 316L parts produced by selective laser melting’, *J. Test. Eval.*, vol. 46, no. 4, pp. 1673–1683, Mar. 2018, doi: 10.1520/JTE20170140.